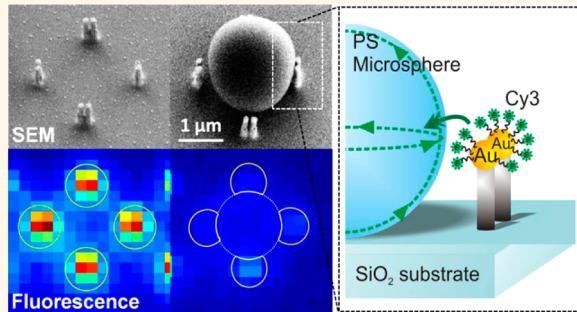


Demonstration of Efficient On-Chip Photon Transfer in Self-Assembled Optoplasmonic Networks

Wonmi Ahn,[†] Yan Hong,[†] Svetlana V. Boriskina,[‡] and Björn M. Reinhard^{†,*}

[†]Department of Chemistry and The Photonics Center, Boston University, Boston, Massachusetts 02215, United States, and [‡]Department of Mechanical Engineering, Massachusetts Institute of Technology, Cambridge, Massachusetts 02139, United States

ABSTRACT Plasmonic nanoantennas facilitate the manipulation of light fields on deeply sub-diffraction-limited length scales, but high dissipative losses in metals make new approaches for an efficient energy transfer in extended on-chip integrated plasmonic circuits mandatory. We demonstrate in this article efficient photon transfer in discrete optoplasmonic molecules comprising gold nanoparticle (NP) dimer antennas located in the evanescent field of a 2 μm diameter polystyrene bead, which served as an optical microcavity (OM). The optoplasmonic molecules were generated through a guided self-assembly strategy in which the OM were immobilized in binding sites generated by quartz (SiO_2) or silicon posts that contained plasmonic nanoantennas on their tips. Control of the post height facilitated an accurate positioning of the plasmonic antennas into the evanescent field of the whispering gallery modes located in the equatorial plane of the OM. Cy3 and Cy5.5 dyes were tethered to the plasmonic antennas through oligonucleotide spacers to act as on-chip light sources. The intensity of Cy3 was found to be selectively increased relative to that of Cy5.5 in the vicinity of the plasmonic antennas where strongly enhanced electric field intensity and optical density of states increase the excitation and emission rates of Cy3 due to spectral overlap with the plasmon. The fluorescent dyes preferentially emitted into the OM, which efficiently trapped and recirculated the photons. We experimentally determined a relative photon transfer efficiency of 44% in non-optimized self-assembled optoplasmonic molecules in this proof-of-principle study.



KEYWORDS: whispering gallery modes · integrated optical circuits · photonic molecules · optical microcavity · plasmonics · fluorescence microscopy · waveguides · hybrid devices

High dissipative losses¹ and lack of significant electro-optical effects in metals define fundamental limitations for the realization of efficient plasmonic devices for signal guiding, modulation, and active information processing on the nanoscale. Different from plasmonic nanoantennas, optical microcavities (OMs) such as dielectric microspheres offer whispering gallery mode (WGM) resonances with extremely long lifetimes and can enhance light–matter interactions through efficient trapping and photon recycling.^{2–6} The high-quality factors of WGMs result, however, primarily from the confinement of the optical modes to the interior of the dielectric resonator, and the electromagnetic field enhancement provided by WGMs is relatively weak when compared to that of plasmonic antennas^{7–9} due to the larger mode volume of the photonic modes. The

complementarity of the electromagnetic properties provided by OMs and plasmonic nanoantennas has triggered significant interest in integrating the two into discrete “optoplasmonic” structures.^{10–19} Photonic–plasmonic mode coupling in hybrid structures comprising both metallic and dielectric resonators could not only mitigate the respective limitations of the individual building blocks but also generate entirely new functionalities.^{17,20} Detailed theoretical analyses of discrete optoplasmonic molecules,²¹ comprising high-Q WGM resonators and an individual gold nanoparticle (NP), revealed that photonic–plasmonic mode coupling is accompanied by an effective electromagnetic field redistribution that results in an effective decrease of cavity mode volume and partial field localization in the vicinity of the NP. The strong localized electromagnetic field in the resulting hot-spot allows

* Address correspondence to bmr@bu.edu.

Received for review March 2, 2013 and accepted April 19, 2013.

Published online April 19, 2013
10.1021/nn401062b

© 2013 American Chemical Society

for a modulation of excitation and emission rates of colocalized quantum emitters,^{22–24} and the additional local density of optical states (LDOS) provided by both the plasmonic and dielectric resonator is expected to enable an efficient resonant light extraction from quantum emitters through coupling to resonances of the hybrid system.^{10,25–27} Furthermore, the contribution of the low-loss WGMs to the total LDOS increases the relative weight of the radiative decay channel over that of the nonradiative decay channels. Consequently, dissipative losses in conventional plasmonic antennas can potentially be reduced by integration into optoplasmonic molecules.

In order to realize the full potential of optoplasmonics, fabrication approaches are required that enable integration of the individual building blocks into defined geometries for an efficient coupling of localized surface plasmon (LSP) modes and high-Q WGMs. The strategies realized thus far include sputtering of gold films,²⁸ direct binding of noble metal NPs or nanorods onto OMs,^{29,30} the manual positioning of plasmonic antennas into the evanescent field of dielectric resonators,³¹ or the *in situ* assembly of optoplasmonic devices by trapping gold NPs in the electromagnetic field associated with WGMs.¹³ Most of these approaches are, however, not compatible with on-chip integration into networks of defined geometry, which is required for functional devices and for interfacing with external peripherals, or risk quenching of the WGMs through the direct attachment of metal NPs onto the OM surface. An alternative rational fabrication approach for discrete optoplasmonic molecules is the template-guided self-assembly of dielectric microspheres into lithographically patterned binding sites defined by gold-NP-tipped posts.³² This approach makes it possible to position plasmonic antennas at defined locations along the entire circumference of the microsphere in the equatorial plane, which is coplanar to the substrate and located half a microsphere diameter above the surface. In this plane, photonic–plasmonic mode coupling can be enhanced in a rational fashion by enclosing the OM with NP supporting posts from multiple sides and by minimizing the separation between the metal NPs and the OM. Indeed, the experimental observation of small but significant TE and TM mode broadening in the experimental scattering spectra of microsphere OMs containing gold NPs in their evanescent field confirmed the coupling between WGMs and LSP modes in this geometry.³² Furthermore, template-guided self-assembly approaches facilitate a systematic variation of the separation between individual OMs in spatially extended 1-D and 2-D arrays. This structural flexibility provides additional control over the photonic coupling between the dielectric resonators.^{33–35}

Theoretical studies¹⁰ have predicted that optoplasmonic molecules support an efficient photon transfer

between quantum emitters localized in the hot-spot of the plasmonic nanoantenna and the WGM resonator. An experimental demonstration of on-chip photon transfer in optoplasmonic molecules is, however, still missing. In this article, we demonstrate that, despite inevitable structural variabilities, self-assembled optoplasmonic molecules achieve an efficient photon transfer between plasmonically enhanced fluorescent light sources and OMs, which is an important step toward on-chip integrated optoplasmonic nanocircuitry. The separation dependence of the energy transfer and the synergistic interplay between plasmonic and photonic building blocks are investigated in detail.

RESULTS AND DISCUSSION

Fabrication and Characterization of Optoplasmonic Molecules.

The fabrication process of the optoplasmonic structures is summarized in Figure 1. Arrays of gold NP dimers were patterned on quartz (SiO_2) or silicon wafers by electron beam lithography, as shown in Figure 1a. The average diameter (d) of the gold NPs was determined as 116.5 ± 9.4 nm, and the gap between the individual gold NPs of each plasmonic dimer antenna was 51.8 ± 10.0 nm. The dimer antennas were arranged in chains of rectangular units with side-centered dimer antennas. Two adjacent units shared one dimer antenna, and the separation between the antennas was slightly larger ($2.08 \pm 0.01 \mu\text{m}$) than the polystyrene (PS) microsphere diameter (D) of $1.98 \pm 0.02 \mu\text{m}$ to facilitate an efficient insertion of the OM in one of the following fabrication steps. Dry etching of the patterned arrays in a reactive ion etching chamber created gold-NP-tipped nanopillars due to removal of the substrate material everywhere except those areas that were protected by the created gold NPs. The tilted SEM image in Figure 1b shows that the height of the created silica nanopillars (h) is $\sim 1 \mu\text{m}$, which positions the gold NPs on their tips in the equatorial plane of the $2 \mu\text{m}$ diameter PS beads. Before insertion of the PS beads into the arrays, the gold NPs were functionalized with 3'-dye-labeled 30 nucleotide long 5'-thiolated single-stranded DNAs. The DNA molecules efficiently self-assemble into a brush on the gold NP surface and serve as a spacer to avoid the quenching of the dye fluorescence through the metal surface.²² The thickness of the DNA brush was determined on a reference gold film as 13.5 nm using ellipsometry. As we will discuss in more detail below, this separation is sufficient to avoid quenching and the plasmonic antennas were found to achieve an efficient enhancement of the fluorescence intensity of the bound dyes. After assembling the dye-functionalized plasmonic antennas, which were intended as on-chip light sources, the assembly of the optoplasmonic structures was completed, as shown in Figure 1c, by integrating PS microspheres through a lateral flow of an aqueous suspension of

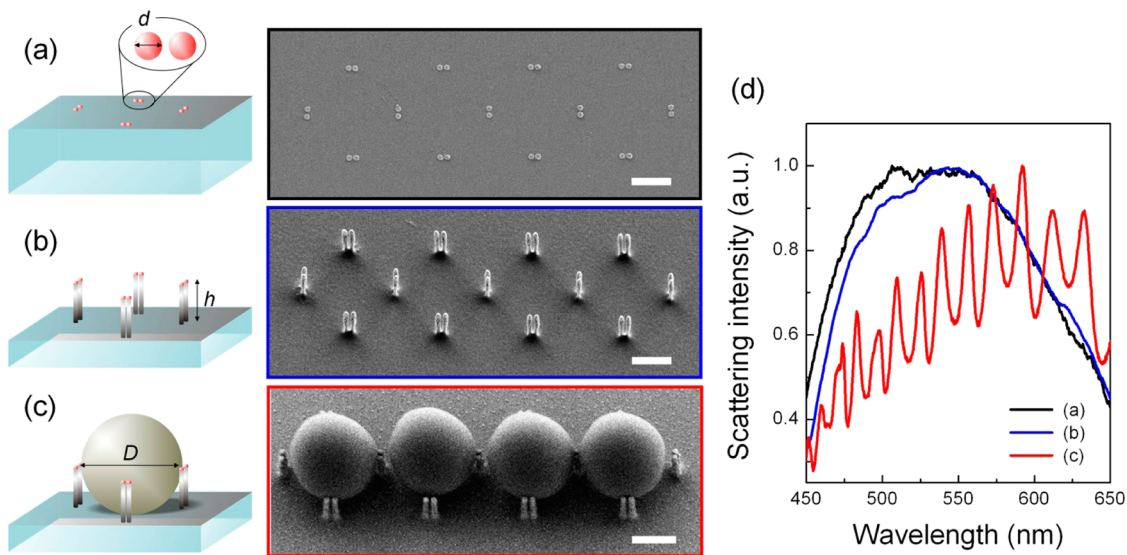


Figure 1. Fabrication process of the hybrid optoplasmonic networks and SEM images at each step of fabrication. (a) Gold dimer disks with a diameter (d) of 116.5 ± 9.4 nm are generated on a quartz or silicon wafer by electron beam lithography. (b) Gold NP dimers on the SiO_2 nanopillars with a height (h) of 0.96 ± 0.07 μm are generated by orthogonal dry etching. (c) PS microspheres (diameter, D , of 1.98 ± 0.02 μm) are inserted into the binding sites defined by the gold posts. The SEM images in (b) and (c) are tilted 30° , and scale bars in all SEM images are $1 \mu\text{m}$. (d) Normalized far-field scattering spectra of (a) gold dimer disks on the substrate, (b) gold NP dimers on the pillars, and (c) completed optoplasmonic arrays.

the microspheres (for detail, please refer to the Methods section).

Figure 1d contains elastic far-field scattering spectra of each fabrication step: (a) gold NP dimers, (b) gold-NP-tipped nanopillars, and (c) completed optoplasmonic structures with PS microspheres in the binding sites. A comparison of spectra (a) and (b) clearly shows that the gold NP dimers exhibit a broad LSPR band in a wavelength range from 450 to 650 nm and that the SiO_2 nanopillars have a negligible effect on the spectral LSPR band. Spectrum (c), however, shows a well-structured spectrum with multiple peaks due to the presence of WGMs provided by the dielectric OM in the completed optoplasmonic structure. Two micrometer diameter PS beads support WGMs that can be directly excited by free-space photons under dark-field illumination. These modes, which have quality (Q) factors between 49.2 ± 10.2 for TE and 64.8 ± 10.3 for TM modes, are significantly sharper than the LSPR mode with which they overlap. The design of the optoplasmonic molecules in Figure 1 fulfills all requirements for photonic–plasmonic mode coupling, and in the following, we will utilize fluorescence microscopy to experimentally validate on-chip photon transfer in these hybrid structures.

Fluorescence Enhancement in Optoplasmonic Molecules. The excitation rate of an emitter with a transition dipole \mathbf{p} is governed by the local field \mathbf{E}_{exc} at the excitation wavelength λ_{exc} : $\gamma_{\text{exc}} \propto |\mathbf{E}_{\text{exc}}(r_0, \lambda_{\text{exc}}) \cdot \mathbf{p}|^2$. We have already demonstrated³² that the local electric field around gold NPs in template-assembled optoplasmonic molecules is dramatically enhanced over that in isolated NP dimers or isolated OMs, thus resulting in the increase of the

excitation rate. The radiative rate of fluorescence dyes can also be enhanced in an optoplasmonic molecule. Provided that the fluorescent dyes are placed in sufficient separation from the metal surface to avoid quenching, the spontaneous emission rate (γ) is predicted to increase with both the local field and the density of optical states. In the weak coupling regime, the spontaneous emission rate is given by $\gamma = (2\omega/3\hbar\epsilon_0)|\mathbf{p}|^2\rho(\mathbf{r}_m, \omega)$, where \mathbf{p} is the transition dipole moment, ρ is the density of photon states, and \mathbf{r}_m is the location of dipole emitter.³⁶ In optoplasmonic molecules, both plasmonic²⁴ and photonic^{25–27} resonances contribute to modify \mathbf{p} and ρ .

We first validated the influence of the plasmonic antennas in the absence of OMs. We used gold NP dimers as plasmonic antennas in this work to achieve an efficient localization of the incident light into electromagnetic hot-spots, where the high density of plasmonic modes facilitates an efficient decay of fluorescence excitation into resonant plasmons. The latter can then efficiently reradiate into free space,^{23,37} resulting in an overall increase in detected fluorescence signal. Since the potential increase in fluorescence intensity provided by plasmonic antennas depends on the exact antenna structure, we first experimentally characterized the fluorescence intensity provided by the NP dimers used in this work. To that end, we fabricated gold NP dimers on quartz substrates, as shown in Figure 1a, and then functionalized those with DNA oligomers carrying either Cy3 or Cy5.5 as dipole emitters. We chose Cy3 whose excitation/emission peak wavelengths of $\lambda_{\text{exc}} = 550$ nm/ $\lambda_{\text{emi}} = 564$ nm overlap with the LSPR band maximum of the gold NP

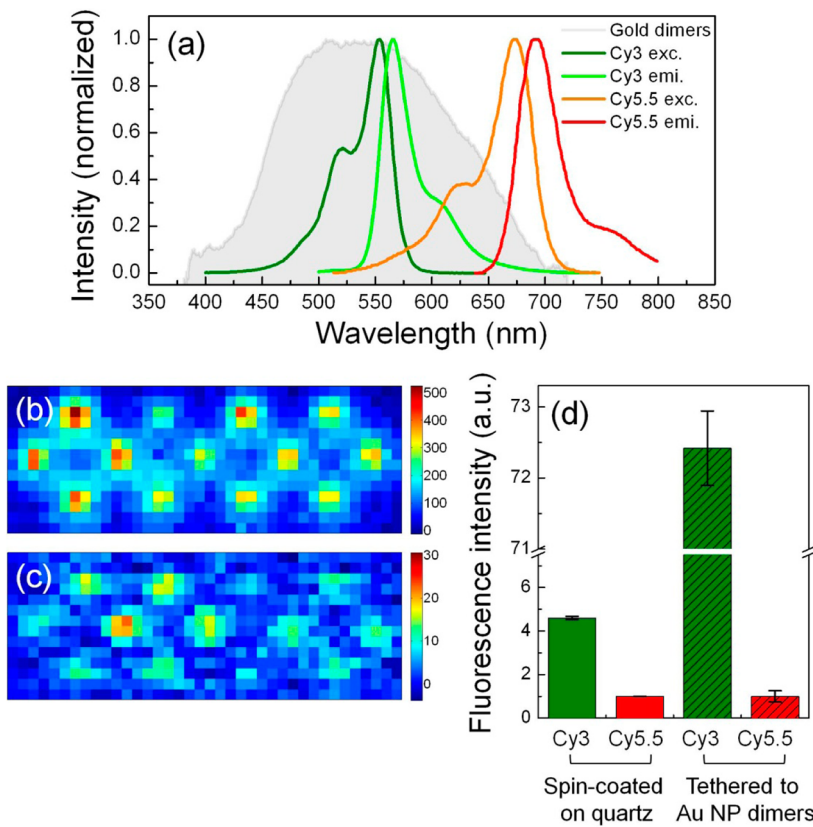


Figure 2. Enhancement of the fluorescence intensity by plasmonic nanoantennas. (a) Normalized far-field scattering spectra of gold NP dimers on a quartz substrate (gray shaded line) and excitation and emission spectra of Cy3 and Cy5.5 (see legends). Fluorescence intensity maps of gold NP dimers functionalized with Cy3 and Cy5.5 are shown in (b) and (c), respectively. Note the difference in scale of the color maps for (b) and (c). (d) Relative fluorescence intensities of equimolar solutions of Cy3- and Cy5.5-functionalized DNAs that were spin-coated on metal-free quartz substrates (left) or tethered to e-beam-fabricated gold NP dimer antennas (right). The Cy5.5 intensities were arbitrarily set to 1. The dimer antennas have the same dimensions as shown in Figure 1a; approximately 60 dimer antennas were analyzed for each dye.

antennas and Cy5.5 whose excitation/emission peak wavelengths $\lambda_{\text{exc}} = 685 \text{ nm}$ / $\lambda_{\text{emi}} = 706 \text{ nm}$ overlap only weakly with the low-energy tail of the LSPR band. The elastic scattering spectra of the plasmonic nanoantennas (gray shaded line) and excitation and emission spectra of two fluorescent dyes³⁸ are shown in Figure 2a. Figure 2b,c shows fluorescence images of representative gold NP dimers functionalized with Cy3 and Cy5.5, respectively. Note the difference in scale of the two color maps in (b) and (c). A systematic comparison of the relative fluorescence intensities of the two dyes when either immobilized on a glass slide by spin-coating or tethered to gold NP dimers via DNA oligomers in Figure 2d shows clearly an increase in Cy3 intensity as a result of the covalent attachment to the plasmonic antennas. The gain in relative fluorescence is characteristic of a selective enhancement of Cy3 excitation and radiative rates through resonant coupling to the plasmons of the dimer antennas.³⁹

In the next step, we applied generalized multi-particle Mie theory (GMT)^{10,40,41} simulations to investigate the possibility of further boosting the radiative rate enhancement, γ_r/γ_r^0 , where γ_r^0 is the radiative rate of a dipole emitter in free space, through assembly of

complete optoplasmonic molecules. In Figure 3a, we compare the simulated radiative rate enhancements for a dipole emitter tethered (i) to an isolated gold NP dimer antenna (blue), (ii) to an isolated OM (gray), and (iii) to a NP dimer antenna located in the equatorial plane of an OM (red) at a separation of 50 nm away from the OM surface. This separation was chosen as a first approximation and allowed us to investigate the underlying physics in the hybrid system. All other antenna dimensions correspond to the measured values given in Figure 1 and its legend. We assumed a separation of 13.5 nm between the emitter and the respective NP or OM surfaces and we averaged over various dipole positions and orientations for each of the three investigated structures. For completeness, we included the enhanced E-field intensity distributions in the optoplasmonic molecules at the resonant peaks marked in Figure 3a with arrows in Figure 3b,c, respectively. The E-field is strongly enhanced in the vicinity of the plasmonic antennas.

The comparison of the calculated γ_r/γ_r^0 values in Figure 3a shows that the plasmonic antenna achieves much stronger radiative rate enhancement than the OM alone, but that the rate enhancement in the

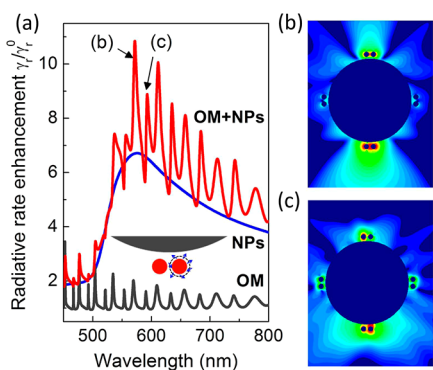


Figure 3. Calculated radiative rate enhancement γ_r/γ_r^0 for a dipole emitter in the vicinity of a gold NP dimer (blue, NP diameter = 116.5 nm, dimer interparticle separation = 51.8 nm), of an OM (gray, 1.98 μm diameter PS microsphere), and of an optoplasmonic molecule comprising the plasmonic antenna in the equatorial plane of the OM (red). The radiative rate enhancement spectra are averaged over various positions and orientations of the dipoles located at a constant separation of 13.5 nm away from the NP or OM surface. The inset shows select dipole positions/orientations marked as blue arrows (NP-OM gap = 50 nm). (b,c) Electric field intensity distributions (log scale) in the OM equatorial plane at the resonant peaks marked in (a).

complete optoplasmonic molecule is even higher. The peak radiative rate enhancement of the optoplasmonic molecule surpasses that of the isolated plasmonic antenna by 63%. The simulations confirm that synergistic interactions between LSPRs and WGMs achieve an additional boost of γ_r/γ_r^0 to beyond what can be accomplished in the separate photonic and plasmonic building blocks. Consistent with our experimentally measured fluorescence intensities for Cy3- and Cy5.5-functionalized plasmonic antennas (Figure 2), we find that the peak of the simulated radiative rate enhancement in the NP gap structure coincides with the peak emission wavelength of Cy3, whereas the radiative rate enhancement at the peak emission wavelength of Cy5.5 is decreased by $\sim 31\%$. This difference in radiative rate enhancement, together with the strong enhancement of excitation rates close to the plasmon resonance, readily accounts for the experimentally observed differences in fluorescence intensities for dye-functionalized plasmonic antennas.

On-Chip Photon Transfer in Optoplasmonic Molecules. Photonic–plasmonic mode coupling³² modifies the excitation and emission rates of quantum emitters, and the GMT simulations of the optoplasmonic molecules studied in this work predict that the radiative rate enhancement remains significantly higher than in conventional plasmonic antennas for antenna–OM separations up to 150 nm (Supporting Information Figure S1). *A priori*, it is not clear whether the proposed template-guided self-assembly approach can generate optoplasmonic molecules with the required precision to achieve a reliable modification of the fluorescence radiative rate and/or emission direction.

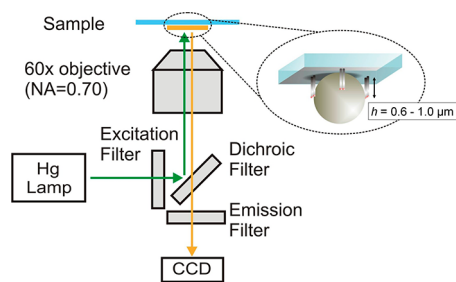


Figure 4. Schematic of the fluorescence microscope used for the spectral characterization of the optoplasmonic molecules. The optoplasmonic array samples were mounted upside-down, so that all of the light collected by the objective had to pass the OMs. Appropriate excitation, dichroic, and emission filters for Cy3 and Cy5.5 were selected (see the Methods section) to record fluorescence images.

We addressed this question experimentally by characterizing the fluorescence intensity of dye-functionalized plasmonic antennas in the presence and absence of OMs. A scheme of the epi-fluorescence experimental setup and sample mounting is shown in Figure 4. For additional details regarding the setup, image acquisition, and processing, please refer to the Methods section. The imaging experiments revealed that the integration of OMs into the binding sites induced a strong change in the fluorescence intensity of the dye-functionalized plasmonic dimer antennas located on the binding site defining posts. As shown in the fluorescence intensity maps in Figure 5, posts in direct vicinity of the OM (a) show significantly lower fluorescence intensities than posts that are more remote to the OM (b). A white dotted line in (a) indicates the location of a PS microsphere in the binding site, and solid yellow lines in (a) and (b) indicate gold NP dimers. The cumulative intensity plots in Figure 5c summarize the fluorescence intensities of a gold NP dimer carrying posts in the presence (red) and absence (blue) of an OM. For both groups, we evaluated ~ 150 gold posts. When the OM is present in the binding sites, the average gold NP dimer–OM separation (G) was determined as ~ 104 nm from multiple SEM images taken at different tilting angles (0–30°; Figure S2). Interestingly, we observed that the gold posts often exhibited a “bending” toward the OMs (Figures S2 and S3) during their convective self-assembly into predefined binding sites, generating short NP antenna–OM gaps. We also verified by SEM that the posts shown in Figure 5 have a height of $\sim 1 \mu\text{m}$ and that the gold NPs were positioned in the equatorial plane of the PS microsphere (Figure S3a,b).

The performed GMT simulations predict a significant enhancement of both E-field intensity and radiative rates in the optoplasmonic molecules. Nevertheless, the experimentally observed fluorescence intensity for posts located in direct vicinity of an OM (Figure 5c, red) is significantly lower than for posts

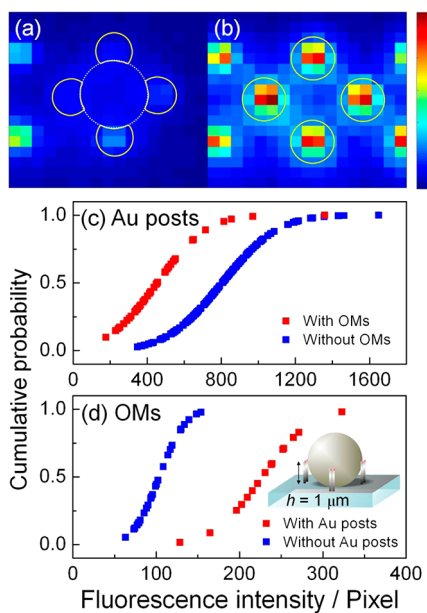


Figure 5. Comparison of fluorescence intensity of Cy3-functionalized gold NP dimer antennas in the presence (a) and absence (b) of an OM. A dotted white circle in (a) indicates the OM inserted into the binding site, and solid yellow circles in (a) and (b) enclose gold posts. Cumulative intensity plots of gold posts (c) and OMs (d) in the presence (red) and absence (blue) of OMs (c) and gold posts (d), respectively. All optoplasmonic structures contain gold NP-functionalized posts with a height of $h = 1 \mu\text{m}$. The inset in (d) illustrates the geometry of the investigated structure.

without an OM (Figure 5c, blue). Directed fluorescence emission into OMs and concomitant excitation of WGMs could explain this apparent contradiction and account for the decrease in fluorescence intensity measured at the post locations. The photons captured by WGMs are recycled in OMs but leak out of the cavity walls eventually and, thus, increase the fluorescence intensity of the OMs. To test this hypothesis, we compared the intensities of OMs embedded in the binding sites containing plasmonic antennas (Figure 5d, red) with those of isolated OMs in the same field of view that were not integrated into post-defined binding sites (Figure 5d, blue). For each condition, we evaluated 15–30 individual OMs. Indeed, consistent with the excitation of WGMs through photons emitted from the fluorescent dyes, the OMs located in direct vicinity to a Cy3-functionalized plasmonic antenna show a systematic increase in fluorescence intensity. The excitation of WGMs is further corroborated by a spatially resolved analysis of the fluorescence intensity across individual OMs. Figure 6a shows the fluorescence intensity map of a substrate-supported OM that is not integrated into an optoplasmonic network. The fluorescence intensity from these reference microspheres is determined by autofluorescence, which leads to an intensity maximum at the center of the microsphere, as depicted in its cross-sectional profile (Figure 6c, blue line). Of particular interest is the

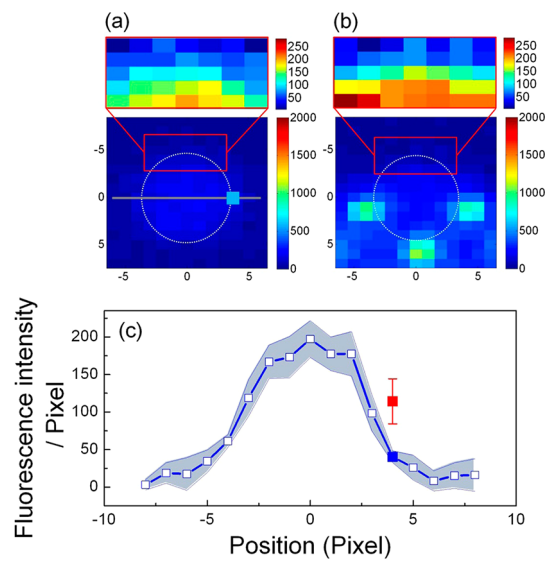


Figure 6. Fluorescence intensity maps of (a) a reference OM without plasmonic antennas and (b) an OM adjacent to three NP dimer carrying posts. The enlarged intensity in the top panel of (a) and (b) shows the rescaled fluorescence intensities of the marked areas with higher contrast. (c) Cross-sectional profile for control OMs without plasmonic antennas (empty blue squares with gray-shaded error areas). The filled blue square refers to the fluorescence intensity at the peripheral position marked in (a) with a blue square. The filled red square reports the average fluorescence intensity measured at the periphery of OMs that are missing a single post. Error bars were calculated from six independent samples.

comparison of this intensity profile with that of OMs, which are not fully integrated into a post-defined binding site but sideways attached to only three posts, as shown in Figure 6b. The fluorescence intensity detected on the side missing a post (filled red square in Figure 6c) is significantly higher than that observed at the periphery of the reference microspheres (filled blue square in Figure 6c). The difference in intensity is also visually apparent in the magnified and for higher contrast rescaled views of these areas in the exemplary structures shown in Figure 6a,b. The increased fluorescence intensity of OMs that are embedded in optoplasmonic molecules when compared with free OMs contained on the same chip confirms that Cy3-functionalized plasmonic antennas inject photons into the OMs where they are efficiently stored due to excitation of WGMs.

In the next step, we further validated that the decreased fluorescence intensity was indeed due to an efficient photon transfer from the Cy3-functionalized plasmonic antenna into the OM and not due to a simple geometric screening effect that perturbs excitation and/or collection. The WGM evanescent field of the substrate-supported PS microspheres used in this work is concentrated in the immediate vicinity of the microsphere surface.^{42,43} We reasoned that a decrease in the post length should increase the separation between the plasmonic antennas and the OM surface

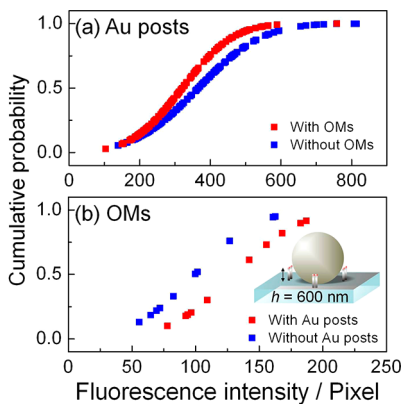


Figure 7. Fluorescence intensities of gold posts and OMs when the height of the post is reduced to $h = 600$ nm (and thus too short to reach the OM equatorial plane). (a) Cumulative intensity for the gold posts in the presence (red) and absence (blue) of the OMs. (b) Corresponding cumulative intensity of OMs. The inset in (b) gives a schematic structure of the investigated optoplasmonic molecules.

and, thus, reduce the photonic–plasmonic mode coupling. The latter would result in a decrease in the relative photon transfer efficiency. In order to test this hypothesis, we fabricated optoplasmonic molecules, with the same overall geometry but with shorter posts. The plasmonic antennas were no longer located in the equatorial plane of the OM but, instead, located ~ 400 nm below the equatorial plane (Figure S3c,d). Due to the geometry of our experimental setup (Figure 4), we only detected light from the microsphere side and all Cy3-emitted photons had to pass the dielectric microsphere to be collected. We analyzed the relative fluorescence intensities obtained from gold posts in the presence and absence of the OMs. The resulting cumulative intensity distribution plots are shown in Figure 7a. The difference in relative fluorescence intensity between the two classes of posts in this case is much weaker than observed for the posts located in the equatorial plane of the OM (see Figure 5c). This difference is also reflected in Student's *t* tests. The two classes of posts (with/without OM) in Figure 5 ($h = 1$ μ m) have a *p* value of <0.001 , while in Figure 7 ($h = 600$ nm), the *p* value has increased to <0.1 . We conclude that the fluorescence intensity of the shortened posts is only weakly affected by the presence of the OM. We also quantified the fluorescence signal emanating from the PS microspheres integrated into optoplasmonic molecules with shortened posts (Figure 7b). The shortening of the post length is accompanied by a substantial reduction in the intensity difference between OMs in the presence (red) and absence (blue) of gold posts, as is evident from comparing the intensity distributions in Figures 5d and 7b. Together, these findings confirm (i) that the differences in observed intensity distributions in Figure 5 are the result of an efficient in-plane photon transfer from the Cy3-functionalized plasmonic dimer

antennas into the OMs, and (ii) that the positioning of the dyes in the equatorial plane of the OM is an absolute requirement for this process to be efficient.

We quantified the relative photon transfer efficiency (η) defined as $\eta = 1 - (I_{+OM}/I_{-OM})$, where I_{+OM} and I_{-OM} indicate the fluorescence intensities of the gold posts in the presence and absence of OMs, respectively, for optoplasmonic molecules with different post heights. These values were obtained by averaging fluorescence intensity values from >150 gold posts. The relative transfer efficiency is 0.44 in the optoplasmonic structures containing the plasmonic antennas in the equatorial plane, but it drops to $\eta = 0.12$ if the posts are reduced in length by 400 nm. Although the presence of the OM can influence the fluorescence excitation and detection efficiencies, this effect applies to η for both post lengths. Our data therefore strongly argue for an enhanced photon transfer efficiency for plasmonic antennas located on posts with a height of 1 μ m. The observation of a relative on-chip photon transfer efficiency of 44% in non-optimized optoplasmonic molecules emphasizes the tremendous potential of optoplasmonic molecules with optimized geometry for radiative rate engineering, long-range photon transfer, and active switching and (de)multiplexing.¹⁰ We emphasize that the current generation of optoplasmonic molecules has room for further systematic improvements since the separation between the plasmonic antennas and the OM in the fabricated structures is with ~ 100 nm still rather large.

CONCLUSION

Photonic–plasmonic mode coupling is a promising strategy for enhancing photon–matter interactions, energy transfer, and signal processing in on-chip integrated optoplasmonic networks beyond the capabilities of both photonic OMs and plasmonic nanoantennas. Our combined experimental and theoretical analyses reveal that plasmonic nanoantennas and OMs interact synergistically to boost not only the transition dipole moment of dyes attached to the plasmonic antennas but also their radiative rates. The emitted light is efficiently captured as OM-trapped recirculating photons. The realization of the full advantage of on-chip integrated optoplasmonic networks hinges on the ability to position dipole-emitter-functionalized plasmonic nanoantennas into the evanescent field located in the equatorial plane of OMs. We achieved a relative photon transfer efficiency of 44% in self-assembled optoplasmonic molecules that contain PS microspheres trapped between silica or silicon posts containing gold dimer antennas on their tips. We validated experimentally that the relative transfer efficiency depends crucially on the height of the NP containing posts in the assembled optoplasmonic structures. The successful combination of significant radiative rate and

E-field intensity enhancement and efficient long-range energy transfer makes optoplasmonic molecules versatile building blocks for on-chip integrated optical networks,

especially if one considers other predicted functionalities of optoplasmonic networks, such as multiplexing,¹⁰ demultiplexing,¹⁰ and all-optical switching.¹⁷

METHODS

Fabrication of Gold-NP-Tipped Nanopillar Cavities. First, regular arrays of dimer nanoholes are patterned in 200 nm thick poly-(methyl methacrylate) (PMMA) layers spin-coated on a quartz or silicon wafer substrate through electron beam lithography (EBL) using a Zeiss SUPRA 40VP scanning electron microscope (SEM) equipped with an Raith Beam Blanker and nanometer pattern generation system (NPGS). A Ti/Au/Cr layer with a thickness of 10/80/35 nm, respectively, was then deposited on the EBL-patterned surface by electron beam evaporation (CHA Industries, Fermont, CA) with deposition rates of 0.5/1.0/0.5 Å/s. A Ti layer improved adhesion of gold films to a quartz or silicon substrate, and a Cr layer protected the gold films from anisotropic dry etch gases. After the PMMA layer was lifted off by washing in acetone, substrates were brought to reactive ion etching (RIE, Plasma-Therm, model 790). The anisotropic etching using a mixture of CHF_3/O_2 (50/5 sccm) at a pressure of 200 mTorr and a power of 150 W removed the quartz or silicon only in exposed areas, which were not protected by Cr layers, resulting in the formation of quartz or silicon nanopillar arrays with Cr layer tips. The height of the nanopillars was controlled through the variation of etching time. To result in $h = 1 \mu\text{m}$ and 600 nm SiO_2 pillars, 7 and 4.5 min of RIE was performed, respectively. To etch a silicon wafer, a mixture of SF_6/Ar (25/25 sccm, 50 mTorr, 200 W, 7 min for $h = 1 \mu\text{m}$) was used instead of CHF_3/O_2 . The layer of Cr was then removed by gentle swirling in a 40 °C solution of Cr etchant for 15 s, and the substrate was rinsed with distilled water thoroughly. Finally, the gold-tipped nanopillars were created with a diameter (d) = $116.5 \pm 9.4 \text{ nm}$, a gap between gold dimers of $51.8 \pm 10.0 \text{ nm}$, and a height of nanopillars (h) = 0.96 ± 0.07 or $0.62 \pm 0.02 \mu\text{m}$.

Functionalization of the Gold NP Dimers with Fluorescently Labeled ssDNA Strands. The arrays of gold-tipped nanopillars were functionalized with dye-labeled 30 bp single-stranded DNAs via a thiol binding. Before incubation, disulfide bonds of thiols in DNA were reduced using TCEP solution (Thermo Scientific Inc.). A drop of 5'-thiolated DNAs ($\sim 15 \mu\text{L}$, 10 μM) that are tagged with 3'-Cy3 or -Cy5.5 was added on the top surface of the prepared gold post substrates and incubated in a dark, humid environment for overnight (sequence: 5' HS AAA AAA AAA AAA AAG GCT GGA GGT TGG TTC ACT Cy3 (or Cy5.5) 3', Integrated DNA Technologies). The excitation/emission wavelengths for Cy3 and Cy5.5 are 550/564 and 685/706 nm, with reported quantum yields of 0.24 and 0.23, respectively.^{38,39} After incubation, the substrate was washed with Tris buffer (10 mM Tris pH 8 and 50 mM NaCl) to remove nonspecifically bound DNAs on the surface, followed by rinsing with DI water to prevent formation of salt crystals on the substrate.

Integration of OMs by Convective Self-Assembly. The regular arrays of dye-tagged gold nanopillar cavities were then used as templates to assemble PS microspheres by a convective self-assembly method. An aqueous solution of PS beads ($1.98 \pm 0.02 \mu\text{m}$ in diameter, 1%; 30 μL) was sandwiched between the patterned nanopillar substrate and a blank quartz substrate separated by a $\sim 380 \mu\text{m}$ gap. Upon evaporation of the water, the meniscus of the microsphere containing solution was dragged across the substrate surface by capillary forces. These forces have a component perpendicular to the patterned surface, which enabled an efficient trapping of microspheres in the cavities formed by the fabricated gold posts. The insertion of microspheres into the dye-tagged gold NP posts completed the assembly of the optoplasmonic molecules for the further fluorescence microscopy.

Fluorescence Microscopy. Fluorescence images of the optoplasmonic molecules were obtained using an inverted microscope (Olympus IX71) equipped with a high-resolution imaging CCD (Andor, iXon^{EM}). A 100 W mercury lamp (Olympus, U-LH100HG) was used as an illumination source, and the image was resolved

using a long working distance $60 \times$ air objective lens (Olympus LUCPLFLN, NA = 0.70). The sample was mounted upside-down, as illustrated in Figure 4. The excited light was efficiently filtered using proper fluorescence imaging filters (excitation/dichroic/emission) for Cy3 ($550 \pm 10/560/580 \pm 10 \text{ nm}$) and Cy5.5 ($650 \pm 10/690/700 \pm 10 \text{ nm}$). The fluorescence images for Cy3 were taken using exposure times of 3 s (10 accumulations), and acquisition conditions for Cy5.5 were adjusted as necessary.

To ensure a direct comparison of the measured fluorescence intensities, we only compared measurements performed under identical conditions on the same chips. The gold posts in the presence and absence of the OM were prepared on the same chip, and their fluorescence intensities were measured under the identical illumination conditions including exposure time, number of accumulation, intensity of light source, etc. Likewise, fluorescence intensities of the OMs with and without gold posts on the same chip were measured under the same acquisition conditions. Since we compared fluorescence intensities under identical conditions, we directly compared total fluorescence intensities without calibration.

Fluorescence Image Analysis. All fluorescence images were processed using custom-written Matlab codes. The fluorescence intensities were background-corrected by subtraction of fluorescence signals taken from an equally sized, but unpatterned neighboring area and normalized by the total area on the detector (25 or 121 pixels) to determine the fluorescence intensity per pixel. To obtain fluorescence intensities from OMs that are integrated in the gold NP dimer cavities, the total fluorescence intensity of the OM was subtracted by the fluorescence intensity from gold NP dimers in the enclosed OM area.

Simulations. We calculate the radiative decay rate γ_r of the dipole \mathbf{p} at the emission wavelength λ_{em} as the power fraction radiated into the far-field by integrating the energy flux through the closed surface surrounding both the dipole and the optoplasmonic molecule.⁴⁴ Generalized multiparticle Mie theory is used for all of the calculations, which provides an exact analytical solution of Maxwell's equations for arbitrary configurations of L metal and/or dielectric spheres.^{10,40,41} The total scattered electromagnetic field is constructed as a superposition of partial fields scattered by each sphere. The incident, partial scattered, and internal fields are expanded in the orthogonal basis of vector spherical harmonics represented in local coordinate systems associated with individual particles: $\mathbf{E}_{\text{sc}}^l = \sum_{(n)} \sum_{(m)} (a_{mn}^l \mathbf{N}_{mn} + b_{mn}^l \mathbf{M}_{mn})$, $l = 1 \dots L$. A matrix equation for the Lorenz–Mie multipole scattering coefficients (a_{mn}^l, b_{mn}^l) is obtained by imposing the continuity conditions for the tangential components of the electric and magnetic fields on the particles surfaces, using the translation theorem for vector spherical harmonics and truncating the infinite series expansions to a maximum multipolar order N . Experimentally obtained gold refractive index values from Johnson and Christy⁴⁵ are used in the simulations.

Conflict of Interest: The authors declare no competing financial interest.

Acknowledgment. This work was supported by the National Science Foundation through Grants CBET-0853798 and CBET-0953121.

Supporting Information Available: Figures S1–S3. This material is available free of charge via the Internet at <http://pubs.acs.org>.

REFERENCES AND NOTES

- Gramotnev, D. K.; Bozhevolnyi, S. I. Plasmonics beyond the Diffraction Limit. *Nat. Photonics* **2010**, 4, 83–91.
- Vahala, K. J. Optical Microcavities. *Nature* **2003**, 424, 839–846.

3. Zhu, J.; Ozdemir, S. K.; Xiao, Y.-F.; Li, L.; He, L.; Chen, D.-R.; Yang, L. On-Chip Single Nanoparticle Detection and Sizing by Mode Splitting in an Ultrahigh-Q Microresonator. *Nat. Photonics* **2010**, *4*, 46–49.
4. Astratov, V. N.; Franchak, J. P.; Ashli, S. P. Optical Coupling and Transport Phenomena in Chains of Spherical Dielectric Microresonators with Size Disorder. *Appl. Phys. Lett.* **2004**, *85*, 5508–5510.
5. Astratov, V. N. Fundamentals and Applications of Microsphere Resonator Circuits. *Photonic Microresonator Research and Applications*, Springer Series in Optical Sciences; Springer: Berlin, 2010; Vol. 156, pp 423–457.
6. Gotzinger, S.; Menezes, L. de S.; Mazzei, A.; Kuhn, S.; Sandoghdar, V.; Benson, O. Controlled Photon Transfer between Two Individual Nanoemitters via Shared High-Q Modes of a Microsphere Resonator. *Nano Lett.* **2006**, *6*, 1151–1154.
7. Busson, M. P.; Rolly, B.; Stout, B.; Bonod, N.; Bidault, S. Accelerated Single Photon Emission from Dye Molecule-Driven Nanoantennas Assembled on DNA. *Nat. Commun.* **2012**, *3*:962, 1–6.
8. Liu, N.; Wen, F.; Zhao, Y.; Wang, Y.; Nordlander, P.; Halas, N. J. Individual Nanoantennas Loaded with Three-Dimensional Optical Nanocircuits. *Nano Lett.* **2013**, *13*, 142–147.
9. Knight, M. W.; Sobhani, H.; Nordlander, P.; Halas, N. J. Photodetection with Active Optical Antennas. *Science* **2011**, *332*, 702–704.
10. Boriskina, S. V.; Reinhard, B. M. Spectrally and Spatially Configurable Superlenses for Optoplasmonic Nanocircuits. *Proc. Natl. Acad. Sci. U.S.A.* **2011**, *108*, 3147–3151.
11. Barth, M.; Schietinger, S.; Fischer, S.; Becker, J.; Nuesse, N.; Aichele, T.; Loeschel, B.; Soennichsen, C.; Benson, O. Nano-assembled Plasmonic–Photonic Hybrid Cavity for Tailored Light–Matter Coupling. *Nano Lett.* **2010**, *10*, 891–895.
12. Zou, S.; Schatz, G. C. Combining Micron-Size Glass Spheres with Silver Nanoparticles To Produce Extraordinary Field Enhancements for Surface-Enhanced Raman Scattering Applications. *Isr. J. Chem.* **2006**, *46*, 293–297.
13. Shopova, S. I.; Rajmangal, R.; Holler, S.; Arnold, S. Plasmonic Enhancement of a Whispering-Gallery-Mode Biosensor for Single Nanoparticle Detection. *Appl. Phys. Lett.* **2011**, *98*, 243104.
14. Fuller, K. A.; Smith, D. D. Cascaded Photoenhancement from Coupled Nanoparticle and Microcavity Resonance Effects. *Opt. Express* **2007**, *15*, 3575–3580.
15. Devilez, A.; Stout, B.; Bonod, N. Compact Metallo-Dielectric Optical Antenna for Ultra Directional and Enhanced Radiative Emission. *ACS Nano* **2010**, *4*, 3390–3396.
16. Hong, Y.; Pourmand, M.; Boriskina, S. V.; Reinhard, B. M. Enhanced Light Focusing in Self-Assembled Optoplasmonic Clusters with Subwavelength Dimensions. *Adv. Mater.* **2013**, *25*, 115–119.
17. Boriskina, S. V.; Reinhard, B. M. Adaptive On-Chip Control of Nano-Optical Fields with Optoplasmonic Vortex Nanogates. *Opt. Express* **2011**, *19*, 22305–22315.
18. Boriskina, S. V.; Povinelli, M.; Astratov, V. N.; Zayats, A. V.; Podolskiy, V. A. Collective Phenomena in Photonic, Plasmonic and Hybrid Structures. *Opt. Express* **2011**, *19*, 22024–22028.
19. Wang, S.; Broderick, K.; Smith, H.; Yi, Y. Strong Coupling between On-Chip Notched Ring Resonator and Nanoparticle. *Appl. Phys. Lett.* **2010**, *97*, 051102.
20. Benson, O. Assembly of Hybrid Photonic Architectures from Nanophotonic Constituents. *Nature* **2011**, *480*, 193–199.
21. Xiao, Y.-F.; Liu, Y.-C.; Li, B.-B.; Chen, Y.-L.; Li, Y.; Gong, Q. Strongly Enhanced Light-Matter Interaction in a Hybrid Photonic–Plasmonic Resonator. *Phys. Rev. A* **2012**, *85*, 031805(R).
22. Anger, P.; Bharadwaj, P.; Novotny, L. Enhancement and Quenching of Single-Molecule Fluorescence. *Phys. Rev. Lett.* **2006**, *96*, 113002.
23. Muskens, O. L.; Giannini, V.; Sanchez-Gil, J. A.; Gomez Rivas, J. Strong Enhancement of the Radiative Decay Rate of Emitters by Single Plasmonic Nanoantennas. *Nano Lett.* **2007**, *7*, 2871–2875.
24. Gersten, J.; Nitzan, A. Spectroscopic Properties of Molecules Interacting with Small Dielectric Particles. *J. Chem. Phys.* **1981**, *75*, 1139–1152.
25. Benner, R. E.; Barber, P. W.; Owen, J. F.; Chang, R. K. Observation of Structure Resonances in the Fluorescence Spectra from Microspheres. *Phys. Rev. Lett.* **1980**, *44*, 475–478.
26. Arnold, S. Cavity-Enhanced Fluorescence Decay Rates from Microdroplets. *J. Chem. Phys.* **1997**, *106*, 8280–8282.
27. Barnes, M. D.; Kung, C.-Y.; Whitten, W. B.; Ramsey, J. M.; Arnold, S.; Holler, S. Fluorescence of Oriented Molecules in a Microcavity. *Phys. Rev. Lett.* **1996**, *76*, 3931–3934.
28. Amarie, D.; Onuta, T.-D.; Potyrailo, R. A.; Dragnea, B. Sub-micrometer Cavity Surface Plasmon Sensors. *J. Phys. Chem. B* **2005**, *109*, 15515–15519.
29. Shopova, S.; Blackledge, C.; Rosenberger, A. Enhanced Evanescent Coupling to Whispering-Gallery Modes Due to Gold Nanorods Grown on the Microresonator Surface. *Appl. Phys. B: Laser Opt.* **2008**, *93*, 183–187.
30. Melnikau, D.; Savateeva, D.; Chuvilin, A.; Hillenbrand, R.; Rakovich, Y. P. Whispering Gallery Mode Resonators with J-Aggregates. *Opt. Express* **2011**, *19*, 22280–22291.
31. Santiago-Cordoba, M. A.; Boriskina, S. V.; Vollmer, F.; Demirel, M. C. Nanoparticle-Based Protein Detection by Optical Shift of a Resonant Microcavity. *Appl. Phys. Lett.* **2011**, *99*, 073701.
32. Ahn, W.; Boriskina, S. V.; Hong, Y.; Reinhard, B. M. Photonic–Plasmonic Mode Coupling in On-Chip Integrated Optoplasmonic Molecules. *ACS Nano* **2012**, *6*, 951–960.
33. Boriskina, S. V. Photonic Molecules and Spectral Engineering. *Photonic Microresonator Research and Applications*, Springer Series in Optical Sciences; Springer: Berlin, 2010; Vol. 156, pp 393–421.
34. Boriskina, S. V. Spectrally Engineered Photonic Molecules as Optical Sensors with Enhanced Sensitivity: A Proposal and Numerical Analysis. *J. Opt. Soc. Am. B* **2006**, *23*, 1565–1573.
35. Yang, S.; Astratov, V. N. Spectroscopy of Coherently Coupled Whispering-Gallery Modes in Size-Matched Bispheres Assembled on a Substrate. *Opt. Lett.* **2009**, *34*, 2057–2059.
36. Novotny, L.; Hacht, B. *Principles of Nano-Optics*; Cambridge University Press: New York, 2006; Chapter 8.
37. Muskens, O. L.; Giannini, V.; Sanchez-Gil, J. A.; Rivas, J. G. Optical Scattering Resonances of Single and Coupled Dimer Plasmonic Nanoantennas. *Opt. Express* **2007**, *15*, 17736–17746.
38. Excitation and emission spectra of Cy3 and Cy5.5 were obtained from www.fluorophores.org.
39. Malicka, J.; Gryczynski, I.; Fang, J.; Kusba, J.; Lakowicz, J. R. Photostability of Cy3 and Cy5-Labeled DNA in the Presence of Metallic Silver Particles. *J. Fluoresc.* **2002**, *12*, 439–447.
40. Xu, Y.-I. Electromagnetic Scattering by an Aggregate of Spheres. *Appl. Opt.* **1995**, *34*, 4573–4588.
41. Mackowski, D. W. Calculation of Total Cross Sections of Multiple-Sphere Clusters. *J. Opt. Soc. Am. A* **1994**, *11*, 2851–2861.
42. Knight, J. C.; Dubreuil, N.; Sandoghdar, V.; Hare, J.; Lefevre-Seguin, V.; Raimond, J. M.; Haroche, S. Mapping Whispering-Gallery Modes in Microspheres with a Near-Field Probe. *Opt. Lett.* **1995**, *10*, 1515–1517.
43. Benson, O.; Gotzinger, S.; Mazzei, A.; Zumofen, G.; Sandoghdar, V.; Menezes, L. de S. *Nanophotonics with Microsphere Resonators*; CRC Press: Boca Raton, FL, 2010; pp 1–29.
44. Kühn, S.; Håkanson, U.; Rogobete, L.; Sandoghdar, V. Enhancement of Single-Molecule Fluorescence Using a Gold Nanoparticle as an Optical Nanoantenna. *Phys. Rev. Lett.* **2006**, *97*, 017402.
45. Johnson, P. B.; Christy, R. W. Optical Constants of the Noble Metals. *Phys. Rev. B* **1972**, *6*, 4370–4379.